Available online at www.sciencedirect.com
SCIENCE DIRECT®
International Journal of Heat and Fluid Flow 25 (2004) 625–635
International Journal of HEAT AND FLUID FLOW
www.elsevier.com/locate/ijhff

Novel MILES computations for jet flows and noise

Paul G. Tucker *

Civil and Computational Engineering Centre, School of Engineering, University of Wales, Singleton Park, Swansea SA2 8PP, UK

Received 19 June 2003; accepted 19 November 2003
Available online 3 February 2004

Abstract

The influence of swirl on jet flow structure and noise is explored. A novel DES (detached eddy simulation) type procedure is tested for a jet with co-flow case. The approach uses a k–l near wall RANS (Reynolds averaged Navier–Stokes) model. Away from walls MILES (monotone-integrated large eddy simulation) is used. Blending of the RANS and MILES regions is achieved using a Hamilton–Jacobi type equation. The MILES solution content enables correct turbulence development on relatively coarse grids. The new hybrid MILES–RANS approach is validated for a plane channel flow. A good law of the wall is gained. For swirling flows, far-field noise levels are essentially calculated using the surface integral of Ffowcs Williams and Hawkings/Curl. Despite MILES use with mostly fourth-order centred differencing, jet turbulence decays excessively downstream. Streamwise vorticity introduced by swirl (unlike with chevrons) increases noise, slightly biasing it to higher frequencies. Lower swirl levels might bring more success. The hybrid MILES–RANS method appears promising. However, for the jet with co-flow case (due to the low co-flow Reynolds number) it is perhaps only very mildly tested.

Keywords: MILES; Jet noise; Swirl; Co-flow; Hybrid modelling

1. Introduction

The accurate prediction of jet flows is important for the reduction of jet engine noise and combustion system performance. Swirling flows have been considered in the context of increased combustion mixing and noise reduction (see Mehta et al., 1991). Often, in aero engines a primary jet is surrounded by a slower moving co-flow giving a velocity difference ΔU. Fig. 1(b) gives an idealisation to this. Evidence suggests (see Morse, 1980) that the initial interaction of the co-flow with the primary has a strong flow structure influence. The work of Papamoschou and Debiasi (2001) indicates that the interaction between the co and core flow also has a profound sound level influence. Various novel devices have recently been considered to reduce jet noise by for example breaking down larger more coherent turbulence structures through the generation of smaller structures. A key example is use of serrated nozzles (chevrons) that are now found on aero engines. Chevrons introduce streamwise vorticity.

The numerical study of the delicate turbulence interactions required to reduce noise is perhaps best carried out through LES (large eddy simulation) related techniques. These are generally not, as with RANS, so dependent on calibration for different flow types. LES has an explicit subgrid scale (sgs) model, a popular one being Smagorinsky's. The sgs model mainly drains turbulence from the resolved scales (however some energy can also be scattered back). Most LES models assume isotropy of the modelled scales. However, with evidence for the existence of worm-vortices characterising the smallest coherent turbulent structures, even with fine grids this assumption is open to question. Also, with LES it is important to ensure the effects of numerical diffusion are insignificant in comparison to the dissipation implied by the LES model. When moving towards realistic engine conditions this poses a serious solution constraint. An LES alternative (sometimes called implicit LES) pioneered by Boris et al. (1992) is MILES. With MILES (monotonically integrated LES), essentially, numerical diffusion is used in place the sgs model.

* Tel.: +44-1792-295255; fax: +44-1792-295598.
E-mail address: p.g.tucker@swansea.ac.uk (P.G. Tucker).

0142-727X/$ - see front matter © 2003 Elsevier Inc. All rights reserved.
doi:10.1016/j.ijheatfluidflow.2003.11.021

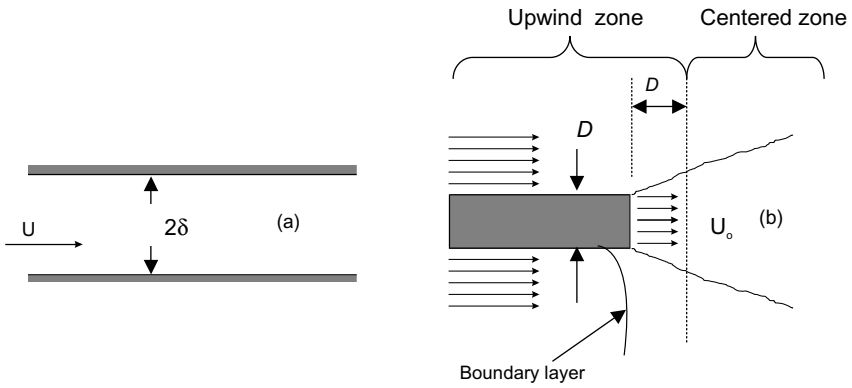

Fig. 1. Geometries considered: (a) plane channel and (b) jet with co-flow.

However, reminiscent of more advanced LES models, MILES can introduce some backscatter (see Rider and Margolin, 2003). Typically, with MILES, following Grinstein and Fureby (2002), the convective flux is discretised as a weighted average of centred and upwind biased components. The upwind component introduces the, sgs model replacing, numerical diffusion that drains turbulence. MILES perhaps has the advantage that the 'sgs modelling' is implicitly anisotropic.

Grinstein and Fureby (2002), show MILES can capture well some complex jet noise vortex dynamics. Shur et al. (2003) make MILES jet noise predictions. The grid used is fine enough to resolve shear layer roll-up. However, a key conclusion of this work was that use of Smagorinsky type LES models results in excessive turbulence transition delay. Such subgrid models perhaps do not have the physics to adequately model the strongly sheared mixing layer region (Kosovic, 1997). [1] In the work of Shur et al., turbulence intensities tend to be under-predicted. This observation also seems to add strength to MILES use, especially when the need for numerical models to deal with realistic engine jet outlet geometries and conditions is born in mind. The work of Shur et al. is extended here in the following two ways: (a) the influence of swirl on flow structure and noise level is explored and (b) a novel zonal LES procedure is tested for a jet with co-flow case. Co-flow cases, for typical aero-engine configurations, involve the modelling of boundary layers (see Fig. 1(b)). These contain LES challenging streak structures requiring fine, computationally expensive, cross-stream grids. Observing this, Spalart (1999) proposed the hybrid DES (detached eddy simulation) method. With this, near walls RANS modelling is used, LES occurring in other regions. Along similar lines, with computational economy in mind, a DES reminiscent novel hybrid MILES approach is proposed here. As in the work of Tucker and Davidson (2003), the novel hybrid MILES approach uses a k–l near wall RANS model. Away from walls MILES is used. This DES like approach is referred to here as a hybrid MILES–RANS method. This new method circumvents near wall streak resolution issues and also perhaps the LES delayed turbulence transition observed by Shur et al. The near wall RANS length scale evaluation involves Eikonal (Sethian, 1999) equation use. This is an exact differential equation for wall distance. Blending of the RANS and MILES regions is achieved by the addition of a Laplacian scaled by normal wall distance (d) to the Eikonal equation. The blending is important. Any discontinuities are likely to introduce spurious noise modes. The new hybrid MILES–RANS approach is initially tested for the Fig. 1(a) plane channel flow. For the swirling flows, far-field jet noise level computations are made. For these, predicted acoustic fluctuations are fed into a simplified version of the surface integral equation of Ffowcs Williams and Hawkings (1969) (FWH). Since the surface is stationary this equation becomes identical to that of Curle (1955). Sound level comparisons are made with the non-swirling flow measurements of Lush (1971) and Tanna (1977). In this way the sound influence of swirl can be better discerned.

2. Numerical method

2.1. Governing equations

To directly capture acoustic waves, as observed by Shur et al., the Navier–Stokes equations should be solved in their compressible form. Conservation of momentum can be expressed using Eq. (1) below:

$$\frac{\partial \rho \tilde{u}_i}{\partial t} + \frac{\partial \rho \tilde{u}_i \tilde{u}_j}{\partial x_j} = -\frac{\partial \tilde{p}}{\partial x_i} + \frac{\partial \tilde{\tau}_{ij}}{\partial x_j} \tag{1}$$

The symbol $\tilde{u}_i$ is a fluid velocity component, ρ density, μ viscosity (evaluated from Sutherland's equation), $\tilde{p}$ sta-

[1] However, it is worth noting that in the shear layer roll-up region Shur et al. include a strong upwind solution component. This, combined with steady jet inflow conditions, might also help explain the delayed transition.

tic pressure, t time and x the spatial co-ordinate. The stress tensor, $\tilde{\tau}_{ij}$, in Eq. (1) is calculated using

$$\tilde{\tau}_{ij} = 2(\mu + \mu_{\mathrm{T}})\left[\tilde{S}_{ij} - \frac{1}{3}\frac{\partial \tilde{u}_j}{\partial x_j}\delta_{ij}\right] \tag{2}$$

where δ_{ij} is the Kronecker delta ($\delta_{ij} = 1$ if $i = j$ and $\delta_{ij} = 0$ if $i \neq j$). The strain rate tensor, $\tilde{S}_{ij}$, is expressed as

$$\tilde{S}_{ij} = \frac{1}{2}\left(\frac{\partial \tilde{u}_i}{\partial x_j} + \frac{\partial \tilde{u}_j}{\partial x_i}\right) \tag{3}$$

The tilde and T subscript in the above equations are used to highlight or help identify that near walls traditional RANS ensemble averaging is assumed and that elsewhere MILES is implemented. Consequently, in the 'RANS' region $\mu_{\mathrm{T}} = \mu_{\mathrm{t}}$, the eddy viscosity. In the MILES zone $\mu_{\mathrm{T}} = \mu_{\mathrm{sgs}} = 0$ i.e. effectively $\mu_{\mathrm{T}} = \mu_{\mathrm{num}}$ the numerical diffusion. In conjunction with the above, just for compressible flow solutions, the following conservation of energy equation is solved

$$\frac{\partial \tilde{E}}{\partial t} + \frac{\partial}{\partial x_j}(\tilde{u}_j(\tilde{E} + \tilde{p})) = \frac{\partial}{\partial x_j}(\tilde{u}_i \tilde{\tau}_{ij}) - \frac{\partial \tilde{q}_j}{\partial x_j} \tag{4}$$

The total energy (internal and kinetic) per unit volume is expressed as

$$\tilde{E} = \rho e + \frac{1}{2}\rho \tilde{u}_i \tilde{u}_i \tag{5}$$

where $e = C_v T$ and C_v is the constant volume specific heat. Pressure, temperature (T) and ρ are related through the equation of state for a perfect gas $\tilde{p} = \rho R \tilde{T}$. For the heat flux q_j the following is used

$$\tilde{q} = -(k + k_{\mathrm{T}})\frac{\partial \tilde{T}}{\partial x_j} \tag{6}$$

In the above, k is the thermal conductivity. Also, $k_{\mathrm{T}} = C_p \mu_{\mathrm{T}}/Pr_{\mathrm{T}}$ where C_p is the specific heat at constant pressure and $Pr_{\mathrm{T}} = 0.9$ is the turbulent Prandtl number. It follows that in the MILES zone since $\mu_{\mathrm{T}} = 0$, $k_{\mathrm{T}} = 0$. The continuity equation to go with the above is

$$\frac{\partial \rho}{\partial t} + \frac{\partial \rho \tilde{u}_j}{\partial x_j} = 0 \tag{7}$$

2.2. Zonal turbulence model details

The modelled turbulent kinetic energy, k, equation is as follows:

$$\frac{\partial \rho k_{\mathrm{T}}}{\partial t} + \frac{\partial \rho \tilde{u}_i k_{\mathrm{T}}}{\partial x_i} = \frac{\partial}{\partial x_j}\left[\left(\mu + \frac{\mu_{\mathrm{T}}}{\sigma_k}\right)\left(\frac{\partial k_{\mathrm{T}}}{\partial x_j}\right)\right] + P_{k_{\mathrm{T}}} - \frac{\rho k_{\mathrm{T}}^{3/2}}{l_\varepsilon} \tag{8}$$

where $P_{k_{\mathrm{T}}}$ is the turbulence production term. For the MILES zone $k_{\mathrm{T}} = k_{\mathrm{sgs}} = 0$. For the RANS region, the k–l model of Wolfshtein (1969) is used where

$$\mu_{\mathrm{T}} = \rho C_\mu l_\mu k_{\mathrm{T}}^{1/2} \tag{9}$$

The length scale in Eq. (9) is

$$l_\mu = C_l \tilde{d}(1 - \mathrm{e}^{-A_\mu y^*}) \tag{10}$$

For Eq. (8) the following is used

$$l_\varepsilon = C_l \tilde{d}(1 - \mathrm{e}^{-A_\varepsilon y^*}) \tag{11}$$

and $y^* = \tilde{d}\rho k^{1/2} C_\mu^{1/4}/\mu$. Constants have the following standard values: $C_\mu = 0.09$, $C_l = 2.4$, $A_\mu = 0.016$, $A_\varepsilon = 0.263$ and $\sigma_k = 1$ (the diffusion Prandtl number for k).

The 'distance' $\tilde{d}$ (again the tilde highlights a variable with two quite different contexts is being used) is evaluated from a Hamilton–Jacobi (HJ) equation (Tucker, 2003)

$$|\nabla \tilde{d}| = 1 + f(\tilde{d})\nabla^2 \tilde{d} + g(d) \tag{12}$$

Here

$$f(d) = \varepsilon_0 \tilde{d} \tag{13}$$

and

$$g(d) = \varepsilon_1 \left(\frac{d}{L}\right)^n \tag{14}$$

The length scale L is the distance from the wall to the MILES region and n is a positive integer. The Eq. (12) left hand side is discretised using first-order Godunov upwind type differences. For the Laplacian, second-order central differences are used. When $\varepsilon_0 = \varepsilon_1 = 0$, Eq. (12) reduces to the hyperbolic natured Eikonal equation. Weak viscosity solutions of this give exact nearest wall distances $d = \tilde{d}$. The Eikonal equation can be solved by propagating fronts from solid surfaces (Sethian, 1999). Here, the equation is propagated towards the RANS/MILES interface. Then at the interface, the condition $d = 0$ is set and Eq. (12) solved using a Newton approach with ε_0, $\varepsilon_1 > 0$. The Laplacian enables a smooth transition between the modelled RANS length scale (that needs an accurate d) and the MILES zone (needing $d = 0$). The function $f(\tilde{d})$ forces the Laplacian to tend to zero near walls. This ensures near wall distances are accurate. The function $g(d)$ controls the RANS length scale in the vicinity of the MILES zone. Fig. 2 (to be discussed more later) gives typical Eq. (12) $\tilde{d}$ distributions for various ε_0 and ε_1 combinations. Despite the simple appearance of the hyperbolic natured Eikonal and Eq. (12), they are not trivial to solve (see Tucker, 2003). For example, transformed equation metric terms need to be discretised using offset metrics. The offset is governed by the front propagation implied in the Eikonal equation.

2.3. Solution of flow governing equations

For the jet cases, the flow governing equations are solved using a modified version of the NTS code of Shur

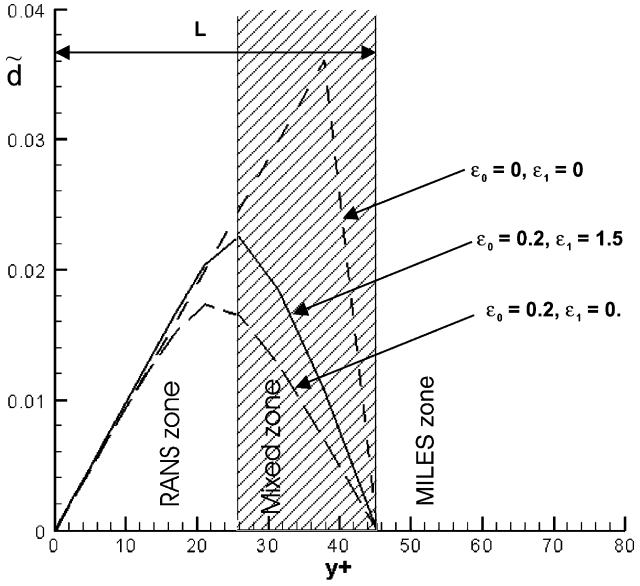

Fig. 2. Hybrid MILES–RANS turbulence length/distance scales.

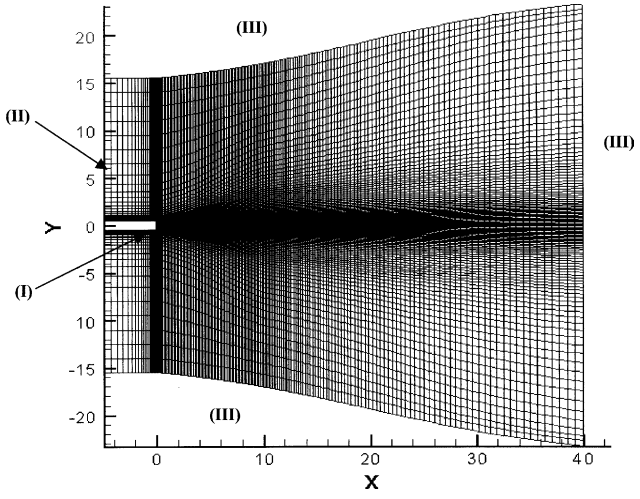

Fig. 3. x–y plane solution grid.

et al. (2003). The problem set-up is virtually identical to that in the paper of Shur et al. Therefore, only brief details are given here. An x–y plane view of the solution grid is shown in Fig. 3. The grid comprises two blocks. The much smaller inner 'axis' block has a radial extent of $\approx$0.2. It is intended to avoid an axis singularity. Since, none of this block's faces are wall adjacent, when solving (12) it is ignored. The total number of grid points is 500,000. At the Fig. 3 boundaries, labelled (**III**), sponges, are applied in the manner of Ashcroft and Zhang (2001). Flow boundaries (**I**) and (**II**) use Dirichlet conditions. Simulated resolved flow inlet turbulence levels are zero. When there is co-flow, the RANS modelled k is set to match the measured value. There is no real resolved turbulence in the RANS zone. Hence, saving computational effort, once converged the k field is frozen. This has similarities to the approach used in Tucker (2004). A hybrid convective flux differencing discretisation is used. The furthest right Fig. 1(b) dashed vertical line, at $X = D$, essentially indicates the key zone where the convective differencing changes. To the right of this line fourth-order centred differencing ($N_{\mathrm{CD}} = 4$) is primarily used in a blended form. To the left, encompassing the MILES zone, fifth-order upwind ($N_{\mathrm{UP}} = 5$) is mostly used. The two are blended using the following equation

$$J_{\mathrm{conv}} = (1 - \alpha)J_{\mathrm{ctr}} + \alpha J_{\mathrm{upw}} \tag{15}$$

where J_{ctr} and J_{upw} are the centred and upwind flux components and α is the blending function. The latter decreases linearly between $X = 0$ and $X = D$ with $\alpha = 1$ at $X = 0$. The smallest $X > D$ usable value of α is 0.25. For $\alpha < 0.25$ the solution in the turbulence acoustic interface becomes highly non-monotonous and hence unusable. A Laplacian based smoothing is used to link the $0 < X \leqslant D$ linearly decreasing α distribution with the constant $\alpha = 0.25$ field. A second-order, three-layer time integration is chosen with a time step $\Delta t = 0.04D/U_0$. To become statistically steady, simulations need $t \cong 2000D/U_0$.

For convenience, for the channel flow predictions the incompressible NEAT code (see Tucker, 2001) is used. The case set-up is virtually identical to that used in Tucker and Davidson (2003) and so only brief details are given here. The (x, y, z) domain size of $2\pi \times 2 \times \pi$ is discretised with a $33\times65\times33$ grid involving a cross-stream (y) geometric grid expansion factor of 1.15. This factor ensures y^+ values at 1st off-wall nodes are around unity. The grid is such that $\Delta x^+ \approx 200$ and $\Delta z^+ \approx 100$. The latter spacing will not allow near wall streak structures to be accurately resolved. The second-order two-layer Crank–Nicolson time integration is chosen. The Δt is such that the maximum and mean Courant numbers (based on streamwise velocities and grid spacings) are 0.14 and 0.075, respectively. Periodic boundary conditions are used in both the streamwise and cross-stream directions. The streamwise flow is maintained by specifying a fixed pressure gradient source term. An LES simulation is performed on this grid using Yoshizawa's (1993) k–l based subgrid scale model with $N_{\mathrm{CD}} = 2$ and $\alpha = 0$. For hybrid MILES–RANS simulations both $N_{\mathrm{CD}} = 2$, $\alpha = 0$ and $N_{\mathrm{UP}} = 3$, $\alpha = 1$ are tried. Results for both are similar.

2.4. Noise postprocessor

The acoustic postprocessor of Shur et al. is used. This yields far-field acoustic pressure fluctuation approximations p'. These approximations are gained from application of the following simplified FWH surface integral theory

$$4\pi|\mathbf{x}|p'(\mathbf{x},t) = \frac{x_j}{|\mathbf{x}|a}\frac{\partial}{\partial t}\left[\int_S \{p'n_j + \rho u_j u_n\}\,\mathrm{d}S\right] + \frac{\partial}{\partial t}\left[\int_S \{\rho u_n\}\,\mathrm{d}S\right] \quad (16)$$

The simplification involves omitting a quadrupole volume integral related source term. This gives dramatic storage savings. It allows time varying data to be stored just at a surface (S) and not through a volume. Quadrupole volume integral omission does not mean that the quadrupole generated noise is not captured. It is still captured through integrals over S. In Eq. (16), u_j are velocity components, u_n is the surface normal velocity, $\mathbf{x}$ the observer position and a the speed of sound. Projections to the outer normal of S are defined by n_j. The terms inside the square brackets are computed at the time when the sound was generated. This 'retarded time' t_r can be expressed as $t_r = t - |\mathbf{x} - \mathbf{y}|/a$ where $\mathbf{y}$ is the field point radius vector. Eq. (16) solution around the three Fig. 4 (FWH 1, FWH 2 and FWH 3) surfaces (S) is considered. These are located where there are no turbulence fluctuations i.e. it is attempted to position the surfaces where fluctuations are purely acoustic and hence the flow irrotational. For this reason, none of the surfaces at $X = 25$ are closed. As noted in the work without co-flow of Shur et al. the lack of closure is a key area of modelling uncertainty. For jets with co-flow, core flow turbulent eddies will be drawn down stream even further. Unless this, co-flow induced, increased eddy convection can be accounted for via some adhoc modelling concept, co-flow will worsen the modelling uncertainty.

Data is stored at surface S at N time intervals of $\Delta\tau$. Therefore, resolved frequencies $f_n = n/N\Delta\tau$, $n = 0, 1, \ldots, N/2$. Here, typically $N = 1000$ and the dimensionless $\Delta\tau = 0.2$. By applying a numerical Fourier transform to Eq. (16), the surface data is converted into the acoustic pressure at $\mathbf{x}$. The pressure at $\mathbf{x}$ is a function of frequency f and the polar angle over S. The acoustic pressure is polar averaged.

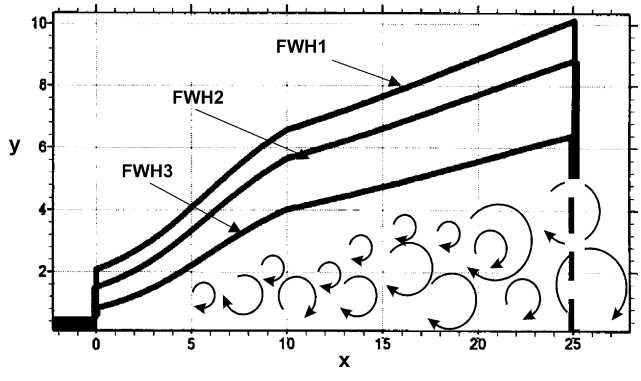

Fig. 4. Locations of FWH surfaces.

3. Discussion of results

3.1. Channel flow cases

Initially the infinite in x and y, Fig. 1a plane channel is considered. Fig. 2 gives the HJ based hybrid MILES–RANS $\tilde{d}$ distributions tested for this geometry. The pure MILES zone is set to start at $y^+ \approx 45$. The short dashed line gives the Eikonal $\varepsilon_0 = \varepsilon_1 = 0$ $\tilde{d}$ solution. As can be seen, $\tilde{d}$ changes abruptly around $y^+ \approx 45$. This is undesirable, potentially introducing spurious acoustic waves. The long dashed line is for $\varepsilon_0 = 0.2$ and $\varepsilon_1 = 0$. The maximum-modelled length scale is now centred between the wall and MILES zone at $y^+ \approx 22.5$. As shown by the full line, increasing ε_1 to 1.5 biases the maximum modelled $\tilde{d}$ towards the MILES zone. Hence the RANS influence in the mixed model region is increased. The mixed model region is reminiscent of the 'DES buffer layer' described by Piomelli et al. (2003).

It might seem most sensible to have the RANS zone extend, without any diminishment of the modelled turbulence, beyond the actual buffer layer and well into the inner logarithmic region. However, experience suggests (Temmerman et al., 2002) that more realistic turbulence statistic results are gained if the RANS region influence is diminished. This is perhaps because MILES zone activity will force resolved scales in the RANS regions. The sum of these resolved and modelled scales will yield excessive turbulence energy. Fig. 5 gives $Re_\tau = 1050$ 'law of the walls' and turbulence statistics for different simulation approaches. The symbols are benchmark LES data of Piomelli (1993). The chain dashed line gives the current LES 'law of the wall.' The Yoshizawa model is used for this prediction. Since, with the present coarse grid, the streak structures cannot be resolved, the LES law of the wall is poor. The Fig. 5a full and dashed lines give results for the Fig. 2 hybrid MILES–RANS profile extremes. These show, inclusion of a near wall k–l RANS model and use of MILES away from walls results in improved agreement. The Fig. 5b turbulence stresses also show encouraging agreement with benchmark data. Predictions have also been made (not shown here) for all the Fig. 2 ε values when the RANS model and interface selection procedure are as prescribed for standard DES. The interface selection procedure results in a greater near wall modelled component extent. However, mean velocity and turbulence statistics again show encouraging agreement with benchmark data.

3.2. Jet flow cases

Four, $Re = 1 \times 10^4$ (based on U_0, the jet outlet velocity and the jet diameter) mostly aero acoustic motivated jet cases are now considered. The Mach number, $Ma = U_0/a_0 = 0.9$ (the '0' subscript on a is used to indicate that this is an ambient condition value).

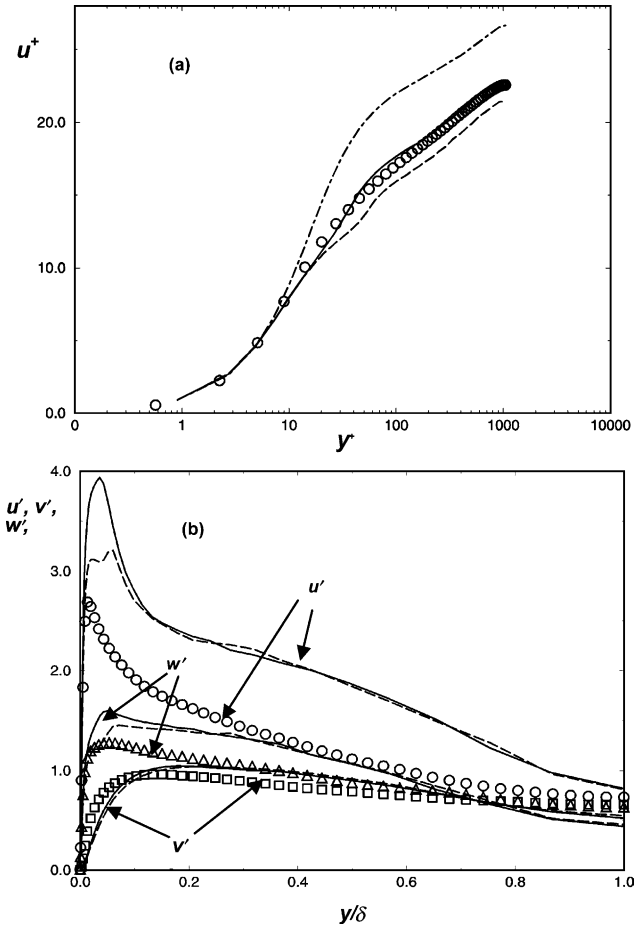

Fig. 5. Plane channel flow: (a) 'law of the wall' and (b) turbulence statistics. (○, Δ, □) 'benchmark' data; (—) $\varepsilon_0 = 0.2$, $\varepsilon_1 = 0$; (– – –) $\varepsilon_0 = \varepsilon_1 = 0$ and (–·–·–) LES.

Where there is swirl, the swirl number, S, is conventionally defined as

$$S = \frac{\int_0^{D/2} uwr^2\,\mathrm{d}r}{D/2\int_0^{D/2} u^2 r\,\mathrm{d}r} \tag{17}$$

where w is the swirl velocity, u axial velocity and r radius. For a linear w distribution, where $w = \Omega r$ (Ω being the fluid's angular velocity), Eq. (17) reduces to $S = \Omega D/(4U_0)$. The cases considered are:

(i) a plane jet with no swirl (i.e. $S = 0$);
(ii) Case (i) with a uniform swirl profile giving $S \approx 0.225$;
(iii) Case (ii) but with the swirl heavily concentrated towards the inlet outer radius and
(iv) Case (i) with co-flow such that $\Delta U/U_0 = 0.27$.

For Case (iii)

$$w = C_0 u C_1^r r^n \cos(\pi r) \tag{18}$$

where $C_0 = 54 \times 10^4$, $C_1 = 2.7182818$ and $n = 15$. For Case (iv) ($\Delta U > 0$), the co-flow velocity and hence turbulence levels are low (0.3%). Therefore, near wall modelling is not strongly tested. However, according to Morse (1980) the co-flow nature at the jet exit exerts a key influence and so it seems sensible to characterise the co-flow boundary layer.

Reflecting HJ computed distances, Fig. 6 gives Case (iv) modelled k contours for a co-flowing jet, hybrid MILES–RANS simulation. The MILES location and ε values are chosen to match those used in Fig. 5 for the plane channel. Fig. 7 gives Case (iv) vorticity contour lines. Frames (a)–(c) are for standard DES, Smagorinsky LES, and the k–l based hybrid MILES–RANS, respectively. As can be seen, for SA DES the transition to turbulence is excessively delayed. The same problem can be observed in the $\Delta U = 0$ work of Shur et al.

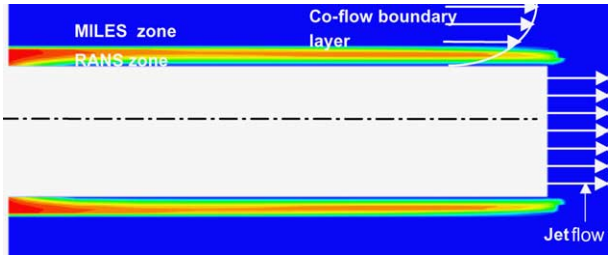

Fig. 6. Modelled k contours for jet with co-flow.

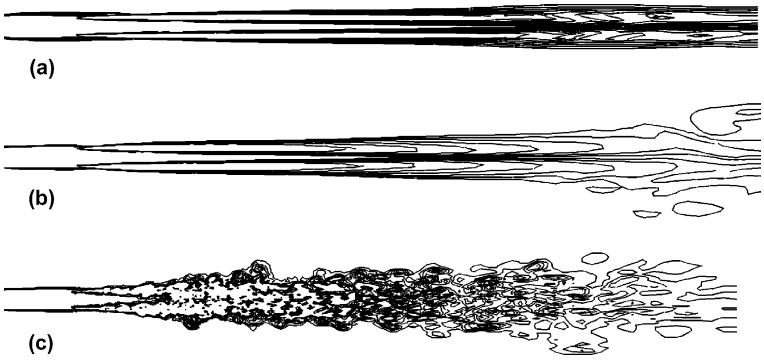

Fig. 7. Case (iv) vorticity contours: (a) DES; (b) Smagorinsky model and (c) hybrid MILES–RANS.

(2003). However, the convective influence of the co-flow, considered here, worsens the problem. As noted earlier, Shur et al. argue that the key cause of the delayed transition is the inadequacy of isotropic LES models in the initial strong shear layer region. Hence Shur et al. (2003) essentially resort to MILES use. However, with fluctuating inlet conditions and centred schemes other workers do not experience this delayed transition problem. Hence the conclusion of Shur et al. might perhaps be extreme with numerical dissipation and the steady inlet condition contributing to the delayed transition.

Fig. 8 compares predicted jet mean velocity and turbulence statistic profiles with measurements. The measurements of Morse (1980) and Mehta et al. (1991) are for $S = 0.2$ and 0.25. Consequently, for the predictions $S \approx 0.225$. Frame (a) compares (normalised by U_0) centre line velocity decay predictions with Morse's measurements. Moving left to right, the three comparison sets correspond to $\Delta U = 0$ with $S \approx 0.225$ (short dashed line and squares), $\Delta U = S = 0$ (long dashed line and circles), and $\Delta U/U_0 = 0.27$, $S = 0$ (full line and triangles). Clearly, $S > 0$ reduces the jet potential core region and co-flow extends it. The larger $S > 0$ discrepancy is partly attributed to the fact that the swirl in the experiment would tend to stagnate the jet axis region flow. The predictions, however, use $u \neq f(r)$. Also, for $S > 0$, there are larger velocity gradients. This will place stronger grid demands. Therefore, for this more challenging turbulence physics case a lower level of agreement is perhaps to be expected. Frames (b)–(d) compare, $S > 0$, $\Delta U = 0$ Case (ii) predictions with measurements for the radial variation of normalised mean axial velocity, normal ($\overline{u'u'}/U_0^2$) stress and shear ($\overline{u'v'}/U_0^2$) stress, respectively. Comparisons are made at $x/D = 1.5$, 2 and 10. The circle, triangle and square symbols are with increasing x/D. The more modern $x/D = 1.5$ measurements are due to Mehta. The others are the popular measurements Morse. Overall the agreement is encouraging. However, the tendency for stress over-prediction adjacent to the jet outlet and under prediction away from it are clear. A finer grid should improve this trait. The excessive drop of predicted turbulence intensities with increasing x/D justifies the proposed reduced dissipation hybrid MILES–RANS approach.

Fig. 9 gives x–y plane vorticity contours for cases (iv), (i) and (ii), respectively. The presentation order is based on the increasing potential core length observation (see Fig. 8(a)). From Frame (a) the potential core region stretching caused by co-flow is clear. The tip of the potential core is a significant noise source and this effect

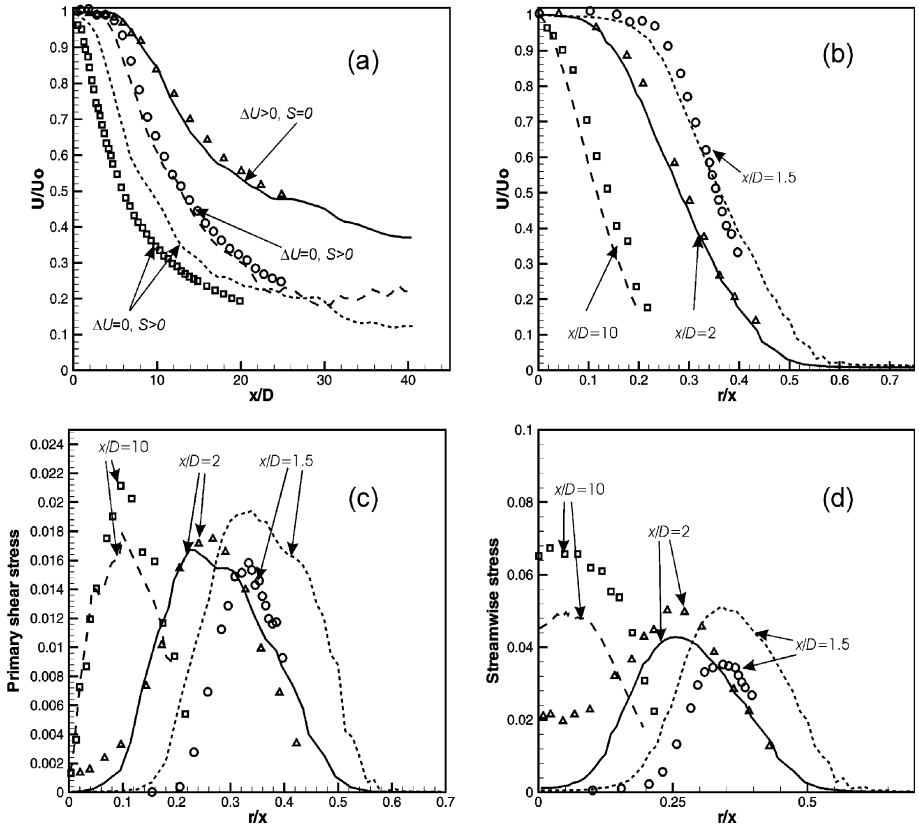

Fig. 8. Jet mean velocity and turbulence statistics profiles for: (a) axial velocity centre line decay; (b) radial variation of axial velocity; (c) radial variation of shear stress and (d) radial variation of normal stress.

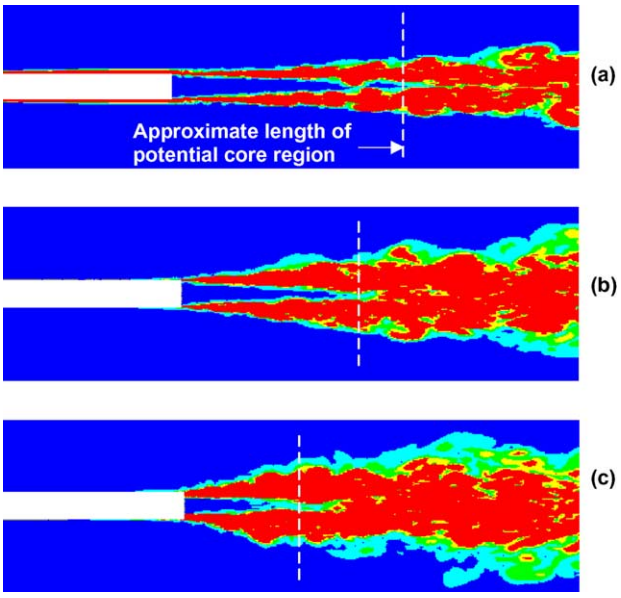

Fig. 9. Instantaneous vorticity plots: (a) co-flow; (b) no-swirl and (c) swirl.

is undesirable. The increasing jet spreading rate and reduction in potential core length for $S > 0$ is evident in Frame (c). For sound reduction the decrease in the potential core length should be useful. However, the question remains regarding whether the effect of reducing the potential core length and other factors outweigh the probable sound increase arising from the higher turbulence production induced by swirl.

Fig. 10 gives a snapshot of the predicted pressure time derivative (indicative of radiated sound) in the r–z plane for $\Delta U = 0$, $S > 0$ and the swirl heavily concentrated towards the jet outer radius (Case (iii)). The contours

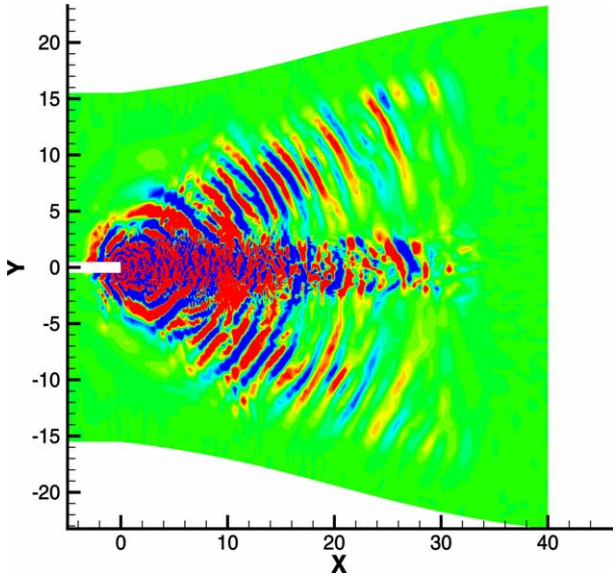

Fig. 10. Case (iii) ($\Delta U = 0$, $S > 0$) pressure time derivative contours.

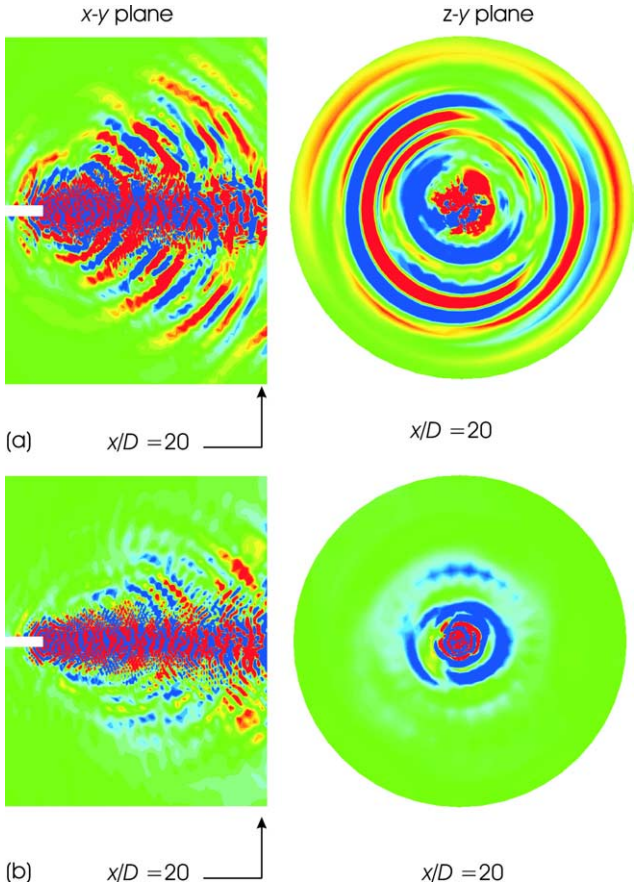

Fig. 11. Pressure time derivative contours in x–y and z–y planes: (a) no co-flow ($\Delta U = S = 0$) and (b) co-flow ($\Delta U > 0$, $S = 0$).

appear very similar to those for $S = 0$. Fig. 11 compares for $S = 0$, the near ($x/D \leqslant 20$) sound field pressure time derivative contours when there is no co-flow (Frame (a)) and co-flow (Frame (b)). The contours for $\Delta U > 0$ suggest the co-flow has a significant acoustic wave blocking influence. This is consistent with the observations of Papamoschou and Debiasi (2001).

Fig. 12 gives z–y plane flow structure information for $x/D = 0.5$. The right hand frames give predicted streak lines and $\tilde{p}$ contours for cases (iii) $S \approx 0.225$, $\Delta U = 0$, (i) $S = 0$, $\Delta U = 0$, and (iv) $S = 0$, $\Delta U/U_0 = 0.27$, respectively. The left-hand frames show the flow visualisation of Ng (2000) for an eight lobed nozzle. The top Frame (a) $S \approx 0.225$ simulation shows clockwise streamwise vorticity regions at the jet edge. Like the streamwise vorticity generated with chevrons, these probably have the potential to break up larger coherent structures and influence sound levels. Streamwise vorticity is also evident in the results of Ng. Interestingly, the non-lobed predictions look similar to the lobed observations of Ng. Frame (b) with $S = \Delta U = 0$ again seems similar the Ng visualisation having contra-rotating vortex pairs. Predictions suggest that the lobes of Ng might not necessarily be the full flow structure-controlling factor—the

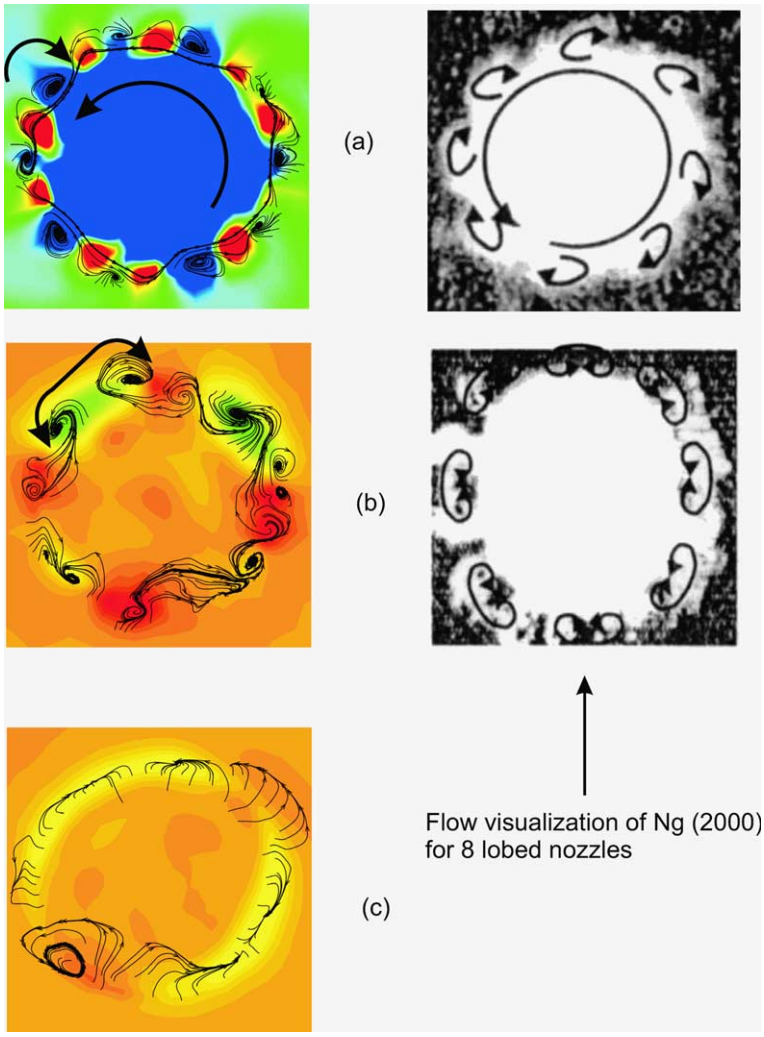

Fig. 12. Flow structure in z–y plane at $x/D = 0.5$ for (a) swirl; (b) no-swirl and (c) co-flow.

general flow features observed by Ng are also present in the simulations. Frame (c) suggests that co-flow substantially reduces streamwise vorticity.

Fig. 13 gives far-field sound level data at $|\mathbf{x}|/D = 120$ for $S = 0$ and $S \approx 0.225$. Frame (a) compares the $S \approx 0.225$ predicted overall sound intensity with the $S = 0$ measurements of Lush (1971) and Tanna (1977). Results are shown for FWH surfaces 1–3. The angle θ is that between the jet axis and observer radius vector. Some sensitivity to the FWH surface configuration can be observed. Predictions for $S = 0$ (see Shur et al. (2003)) are in agreement with the measurements of Lush and Tanna. Therefore, it can be concluded from Frame (a) that the present swirl level has increased noise. Frame (b) gives sound pressure level (SPL) power spectra for $\theta = 30°$ with just FWH2. The dimensionless frequency $St = fD/U_0$. For $St < 1$, results for the three FWH surfaces are similar. Due to grid resolution demands, for higher St, results deviate. The $St > 1.5$ tones, especially evident for the $S > 0$ predictions, are again probably mostly due to grid resolution demands. The lower frequency $St \approx 1.5$ tone is evident in both the $S = 0$ and $S > 0$ results. Shur et al. indirectly attribute this spurious tone to delayed turbulence transition in the shear layer roll up region. This delay could be attributed to the significant upwind differencing component in this region and the lack of inlet forcing. However, even with these uncertainties, it is clear that swirl has shifted noise to higher frequencies. The successful chevron approach prior to tuning also produced more noise. Careful tuning with respect to swirl profile and level could be required to ensure the added turbulence correctly modifies larger coherent structures.

The work of Papamoschou and Debiasi (2001) suggests that with co-flow, reduction of the potential core extent gives noise reductions. This is because the end of potential core region is a major noise source. Shortening this region maximises the co-flows sound shielding potential. As the results here show, swirl has the desirable property of shortening the potential core region.

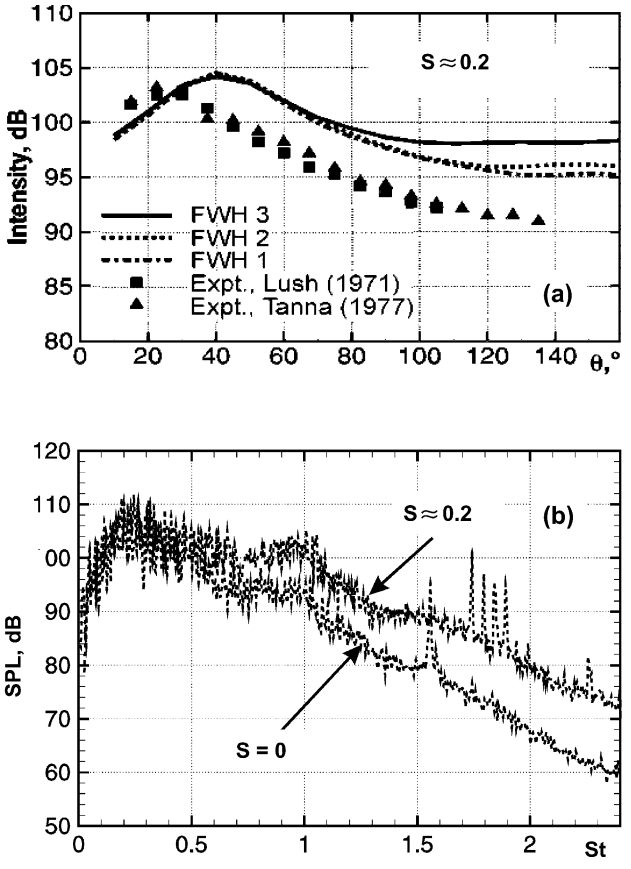

Fig. 13. Far-field noise data at $|\mathbf{x}|/D = 120$: (a) overall sound intensity and (b) $\theta = 30°$ SPL power spectra.

Therefore, exploring the effect of swirl when there is co-flow seems worthwhile and will hopefully be the subject of future work. However, the $\Delta U \neq 0$ FWH surface integral implementation would need consideration. The swirl levels used here are extreme being selected to allow comparison with available experimental data. If used in a real engine the present swirl levels would produce a significant thrust loss. Worthwhile future work might involve studying lower swirl levels and different swirl profiles with co-flow.

4. Conclusions

The influence of co-flow and swirl on flow structure and jet noise was explored. The jet Reynolds number was 1×10^4. A novel hybrid MILES–RANS procedure was tested for a plane channel and jet with co-flow. Blended RANS/MILES region implied turbulence length scales were computed using a Hamilton–Jacobi equation. The blending is important. Discontinuities are likely to introduce spurious noise modes. For the channel, a good law of the wall was gained with no parameter tuning. Despite MILES use jet turbulence still had excessive downstream decay. The streamwise vorticity introduced by swirl increased noise. Further swirl profile/level optimisation work in conjunction with a co-flow might be worthwhile along with co-flow studies. The hybrid MILES–RANS method appears promising. However, for the jet with co-flow case it was only very mildly tested.

Acknowledgements

This work was carried out at Boeing Commercial Airplanes Seattle. I would like to thank the Royal Academy of Engineering for the Global Research Award that primarily made this visit possible and also Boeing for their funding assistance. Also, I would like to thank P. Spalart, M. Shur and M. Strelets for their kind help and the use of their excellent code.

References

Ashcroft, G., Zhang, X., 2001. A computational investigation of the noise radiated by flow induced cavity oscillations. AIAA Paper, AIAA 2001-0512.

Boris, J.P., Grinstein, F.F., Oran, E.S., Kolbe, R.L., 1992. New insights into large eddy simulation. Fluid Dyn. Res. 10, 199–228.

Curle, N., 1955. The influence of solid boundaries on aerodynamic sound. Proc. Roy. Soc. (London), Series A 231 (1187), 505–514.

Ffowcs Williams, J.E., Hawkings, D.L., 1969. Sound generation by turbulence and surfaces in arbitrary motion. Phil. Trans. Roy. Soc. London, Series A 264 (8), 321–342.

Kosovic, B., 1997. Subgrid scale modelling for the large eddy simulation of high Reynolds number boundary layers. J. Fluid Mech. 336, 151–182.

Grinstein, F.F., Fureby, C., 2002. Recent progress on MILES for high Reynolds number flows. ASME J. Fluids Eng. 124 (December), 848–861.

Lush, P.A., 1971. Measurements of subsonic jet noise and comparison with theory. J. Fluid Mech. 46 (Pt. 3), 477–500.

Mehta, R.D., Wood, D.H., Clausen, P.D., 1991. Some effects of swirl on turbulent mixing layer development. Phys. Fluids A 3 (11).

Morse, A.P., 1980. Axisymmetric turbulent shear flows with and without swirl. Ph.D. Thesis University of London.

Ng, T.T., 2000. Visualisation study of a passively perturbed swirling jet. AIAA J., Technical Notes 39 (1), 188–190.

Papamoschou, D., Debiasi, M., 2001. Directional suppression of noise from a high-speed jet. AIAA J. 39 (3), 380–387.

Piomelli, U., 1993. High Reynolds number calculations using the dynamic subgrid-scale stress model. Phys. Fluids 5, 1484–1490.

Piomelli, U., Balaras, E., Squires, K.D., Spalart, P.R., 2003. Interaction of the inner and outer layers in large-eddy simulations with wall-layer models. Int. J. Heat Fluid Flow 24, 538–550.

Rider, W.J., Margolin, L., 2003. From numerical analysis to implicit subgrid turbulence modelling. AIAA Paper, AIAA 2003-4101.

Sethian, J.A., 1999. Fast marching methods. SIAM Rev. 41 (2), 199–235.

Shur, M.L., Spalart, P.R., Strelets, M.Kh., Travin, A.K., 2003. Towards the prediction of noise from jet engines. Int. J. Heat Fluid Flow 24, 551–561.

Spalart, P.R., 1999. Strategies for turbulence modelling and simulations. Proc. 4th Int. Symp. Eng. Turbulence Modelling and Measurements, Ajaccio, Corsica, France, pp. 3–17.

Tanna, H.K., 1977. An experimental study of jet noise. Part I: Turbulent mixing noise. J. Sound Vib. 50 (3), 405–428.

Temmerman, L., Leschziner, M.A., Hanjalic, K., 2002. A-priori studies of a near-wall RANS model within a hybrid LES/RANS scheme. In: Rodi, W., Fueyo, N. (Eds.), Engineering Turbulence Modelling and Experiments, vol. 5. Elsevier Science, pp. 317–326.

Tucker, P.G., Davidson, L., 2003. Zonal *k–l* based large eddy simulations. Comput. Fluids 33, 267–287.

Tucker, P.G., 2001. Computation of unsteady internal flows. Kluwer Academic Publishers, Dordrecht.

Tucker, P.G., 2003. Differential equation based distance computations for DES and RANS. J. Computat. Phys. 190 (1), 229–248.

Tucker, P.G., 2004. Hybrid MILES–RANS method for more dissipative solvers and the use of non-linear LES. AIAA Paper AIAA-2004-0071.

Wolfshtein, M., 1969. The velocity and temperature distribution in one-dimensional flow with turbulence augmentation and pressure gradient. Int. J. Heat Mass Transfer 12, 301–318.

Yoshizawa, A., 1993. Bridging between eddy-viscosity-type and second order models using a two-scale DIA. 9th Int. Symp. Turbulent Shear Flow, Kyoto 3, 23.1.1–23.1.6.